Asymmetrical C-C Coupling for Electroreduction of CO on Bimetallic Cu-Pd Catalysts

*Hao Shen[1, ‡], Yunzhe Wang[2, ‡], Tanmoy Chakraborty[2], Guangye Zhou[1], Canhui Wang[1], Xianbiao Fu[1], Yuxuan Wang[1], Jinyi Zhang[1], Chenyang Li[2], Fei Xu[1], Liang Cao[2], Tim Mueller[2, *], Chao Wang[1, 3, *]*

[1] Department of Chemical and Biomolecular Engineering, Johns Hopkins University, Baltimore, Maryland 21218, United States

[2] Department of Materials Science and Engineering, Johns Hopkins University, Baltimore, Maryland 21218, United States

[3] Ralph O'Connor Sustainable Energy Institute, Johns Hopkins University, Baltimore, Maryland 21218, United States

KEYWORDS

CO_2 reduction, CO reduction, asymmetric C-C coupling, electrocatalysis, Cu-Pd bimetallic alloy catalysts

ABSTRACT

Electroreduction of carbon monoxide (CO) possesses great potential for achieving the renewable synthesis of hydrocarbon chemicals from CO_2. We report here selective reduction of CO to acetate using Cu-Pd bimetallic electrocatalysts. High activity and selectivity are demonstrated for CO-to-acetate conversion with >200 mA/cm^2 in geometric current density and >65% in Faradaic efficiency. An asymmetrical C-C coupling mechanism is proposed to explain the composition-dependent catalytic performance and high selectivity toward acetate. This mechanism is supported by the computationally predicted shift of the *CO adsorption from the top-site configuration on Cu (or Cu-rich) surfaces to the bridge sites of Cu-Pd bimetallic surfaces, which is also associated with the reduction of CO hydrogenation barrier. Further kinetic analysis of the reaction order with respect to CO and Tafel slope supports a reaction pathway with *CO-*CHO recombination following a CO hydrogenation step, which could account for the electroreduction of CO to acetate on the Cu-Pd bimetallic catalysts. Our work highlights how heteroatomic alloy surfaces can be tailored to enable distinct reaction pathways and achieve advanced catalytic performance beyond monometallic catalysts.

INTRODUCTION

Electrochemical reduction of carbon dioxide is promising for mitigation of carbon emissions and building up carbon-neutral energy infrastructures.[1, 2] Electrolytes of high alkalinity are known to favor C-C coupling in this process, a key step toward value-added multi-carbon (C_{2+}) products such as ethylene, ethanol, acetate and *n*-propanol.[3, 4] However, the undesired side reaction with CO_2 has limited the practical implementation of alkaline electrolytes in CO_2 electrolyzers.[5] This challenge can be circumvented by sequential electroreduction of CO_2 to CO and then CO to C_{2+}.[6-12] While the former step can be carried out at >90 % Faradaic efficiency (FE) in bicarbonates (e.g., $KHCO_3$)[13-18], the latter is compatible with alkaline electrolytes such as KOH and allows for taking advantage of the high alkalinity to enhance C_{2+} selectivities.[10, 19-24] Electroreduction of CO has thus gained increasing attention for renewable synthesis of hydrocarbon chemicals.[25]

Copper (Cu) has been the sole metal known for favoring C_{2+} products in CO electroreduction (this also holds true to CO_2 electroreduction).[6, 11, 26] The rate of C_{2+} production is typically limited by the C-C coupling step between adjacent *CO(H) adsorbates, which is sensitive to the surface structure of Cu.[19, 20, 26] Multiple reaction pathways can co-exist on Cu surfaces with shared rate-determining steps (RDSs), limiting the selectivity toward a specific C_{2+} product.[9, 11] To overcome this challenge, alloying Cu with another transition metal (e.g., Au,[27, 28] Ag,[29-31] Pd,[32] etc.) has been investigated for CO (and CO_2) reduction electrocatalysis. In alloy catalysts, the heteroatomic interactions between the dissimilar metals can be utilized to modify the surface adsorption properties and reactivities via geometric and electronic effects.[33-35] The alloy electrocatalysts studied for CO_2 and CO reduction, however, have largely been limited to

those conventional alloys without control over the surface atomic ensembles, for which the mechanistic understanding has focused on nanoscale mophological[31, 32, 36, 37] or strain[27, 30] effects. The lack of atomically resolved interpretation of active sites and reaction pathways on bimetallic surfaces has impeded the development of alloy electrocatalysts with substantially superior performance than monometallic Cu.

We report here bimetallic Cu-Pd alloys as advanced electrocatalysts for selective reduction of CO to acetate. Surfactant-free Cu-Pd nanocrystals were synthesized with control over the composition and applied for electrocatalytic studies by using gas-diffusion electrodes and flowing alkaline catholytes. The catalytic activity and selectivity toward different C_2 products were systematically studied and correlated to the alloy composition. Density functional theory (DFT) calculations and kinetic studies were combined to interpret the relationship between alloy composition and catalytic performance. Our findings feature distinct catalytic mechanisms of the bimetallic electrocatalysts for CO reduction in comparison to monometallic copper.

RESULTS AND DISCUSSION

Cu-Pd nanocrystals of three different compositions (with elemental ratio of 70:30, 49:51, and 23:77; **Table S1**) were synthesized by adopting a surfactant-free approach previously reported by Ma *et al*.[32] The derived products presented an agglomerated form and have particle sizes in the range of ca. 10-30 nm (**Figures 1a** and **S1-S4**). This was in line with the size and morphology of the Cu and Pd controls prepared in a similar way. High-resolution transmission electron microscopy (HRTEM) images show polycrystalline nanostructures with crystal domains on the

sub-10 nm scale for all of the three alloy compositions (**Figure 1b-d**). Element mapping based on energy-dispersive X-ray spectroscopy (EDX) displayed uniform distribution of both Cu and Pd throughout the bimetallic nanostructures, confirming the formation of homogeneous alloys (**Figure 1c-e**). This was confirmed by the X-ray diffraction (XRD) patterns collected on the bimetallic nanocrystals, which exhibit the features of single face-centered cubic (fcc) phase (**Figure S5**). It is noted that thermal annealing to introduce phase ordering (or formation of intermetallic phase) was avoided to prevent nanocrystal aggregation or agglomeration and loss of active surface areas.[32]

Electrocatalytic performance of the bimetallic Cu-Pd electrocatalysts for CO reduction was evaluated using a three-compartment gas-diffusion electrode (GDE) cell.[38] The three bimetallic electrocatalysts delivered similar current densities, *e.g.*, 191, 211 and 206 mA/cm^2 at −1.0 V (versus reversible hydrogen electrode, RHE; the same potential scale is used in following discussion unless otherwise specified) for $Cu_{70}Pd_{30}$, $Cu_{49}Pd_{51}$ and $Cu_{23}Pd_{77}$, respectively (**Figures 2** and **S6**). In comparison, the Cu control gave a current density of 193 mA/cm^2 at this potential. Ethanol and acetate were the primary products obtained with $Cu_{70}Pd_{30}$ (**Figure 2b**). Ethanol was consistently detected at >14% Faradaic efficiency (FE) at potentials more negative than −0.5 V, while the yield of acetate exhibited gradual increase with overpotential, from 20% at −0.5 V to 29% at −1.2 V. The $Cu_{49}Pd_{51}$ catalyst produced acetate dominantly throughout the investigated potential range (**Figure 2c**). In this case, the CO-to-acetate conversion had an onset potential of −0.4 V and the corresponding FE was found to be consistently above 50% from −0.7 V to −1.2 V. At −1.2 V, >65% FE toward acetate was achieved, while the other CO reduction products (ethanol, ethylene, and methane) had a total FE of <10%. This selectivity of $Cu_{49}Pd_{51}$ toward acetate even surpassed the performance of Cu nanosheets, which was previously reported

for favoring acetate production from CO reduction.[39] For the Pd-rich catalyst ($Cu_{23}Pd_{77}$), the hydrogen evolution reaction (HER) became dominant in the electrocatalytic process and occupied >40% FE throughout the investigated potential region. Acetate was also detected as the primary product of CO reduction, but with lower FEs than that of $Cu_{49}Pd_{51}$, *i.e.*, at ca. 20-30 % from −0.5 V to −1.2 V (**Figure 2d**). Ethanol was the only other CO reduction product detected at significant amounts, with a peak FE of 14% obtained at −0.9 V. In comparison, ethylene and ethanol were found to be the major CO reduction products from the Cu control, with the peak FEs reaching 38% (at −0.8 V) and 25% (at −1.2 V), respectively, whereas acetate was detected as a minor product with a maximum FE of 6.1% (at −1.1 V) (**Figure 2a**). Pure Pd, on the other side, was found to be inactive for CO reduction and only produced H_2 under similar reaction conditions (**Figure S7**). It can be seen that, while the Cu- ($Cu_{70}Pd_{30}$) and Pd-rich ($Cu_{23}Pd_{77}$) catalysts resemble pure Cu and Pd, respectively, to a large extent, the intermediate composition ($Cu_{49}Pd_{51}$) gave distinct behaviors that selectively reduce CO to acetate.

The composition-dependent electrocatalytic performance of Cu-Pd can be better visualized by comparing the FEs and partial current densities for C_{2+} products (**Figure 3** and **Figure S8**). At −1.0 V, $Cu_{49}Pd_{51}$ delivered 163 mA/cm^2 of geometric current density toward acetate, ethylene and ethanol in total (J_{C2+}, **Figure S8a**). This was only slightly higher than Cu, which had a J_{C2+} of 128 mA/cm^2. They were followed by $Cu_{70}Pd_{30}$ and $Cu_{23}Pd_{77}$, which had J_{C2+} of 103 and 68 mA/cm^2 at this potential, respectively. Since the total reaction current densities were quite consistent among the five catalysts, the trend in terms of FE toward C_{2+} products, FE_{C2+}, followed a similar trend, namely $Cu_{49}Pd_{51}$ > Cu > $Cu_{70}Pd_{30}$ > $Cu_{23}Pd_{77}$ > Pd (**Figure 3a**). The high FE_{C2+} of $Cu_{49}Pd_{51}$ arose from its high selectivity toward acetate. The dependence of partial current density ($J_{acetate}$) and Faradaic efficiency ($FE_{acetate}$) for acetate production on the

alloy composition exhibited a "volcano" shape as the content of Pd increases (**Figure 3b**). $J_{acetate}$ increased from 11.0 mA/cm^2 with Cu to the peak value of 144.7 mA/cm^2 with $Cu_{49}Pd_{51}$, and then dropped to 53.9 mA/cm^2 for $Cu_{23}Pd_{77}$. Correspondingly, $FE_{acetate}$ elevated from 5.7% for Cu to 65.2% for $Cu_{49}Pd_{51}$. In contrast to the case for acetate, the production of ethylene decreased monotonically in terms of both partial current density and FE at increasing Pd content (**Figure 3c**). While Cu delivered 30.2% of $FE_{ethylene}$ and 58.4 mA/cm^2 of $J_{ethylene}$ at −1.0 V, these values drastically dropped to 5.3% and 10.2 mA/cm^2 for $Cu_{70}Pd_{30}$. The yields of ethylene were even lower on the more Pd-rich catalysts. The case for ethanol seems to sit between the situations for acetate and ethylene, for which Cu and $Cu_{70}Pd_{30}$ had rather similar performances and $FE_{ethanol}$ of ~20%, in comparison to ~5% for $Cu_{49}Pd_{51}$ and $Cu_{23}Pd_{77}$ (**Figure 3d**).

It is noted that, although the above discussions of electrocatalytic performance are based on the geometric current densities (**Figures 3** and **S8**), similar conclusions can also be drawn from the specific activities, due to rather consistent electrochemically active surface areas (ECSAs) for the involved catalysts prepared using similar methods (**Figures S9-S11**). Post-reaction analysis of the surface composition indicates that the coverages of Cu and Pd largely follow the elemental ratio of the bulk, in line with the expectation from homogeneous, random alloys (**Figure S12**). The stability of the $Cu_{49}Pd_{51}$ was also examined continuously at -1.0V vs. RHE for over 30 hours in 1 mol/L KOH (**Figure S13**). The result shows a stable and undiminished current density (>200 mA/cm^2) in CO electroreduction and the selectivity towards acetate was kept over 50% during the test period. Post-reaction characterization combining XRD (**Figure S14**), HRTEM (**Figure S15**), and EDX-based element mapping (**Figure S16**) confirmed the stability of the alloy catalysts in terms of both morphology and crystal phase.

The composition-dependent product distribution points to a different catalytic mechanism on the Cu-Pd bimetallic surfaces from the corresponding situation on pure Cu. Noticeably, such a phenomenon was not reported in the previous studies of CO_2 reduction on similar Cu-Pd electrocatalysts, where CO was found to be the dominant product.[32, 40] Electron-transfer mediated *CO-*CO dimerization has been generally accepted as the C-C coupling mechanism for the electroreduction of CO to C_{2+} hydrocarbons on Cu surfaces.[8, 41-43] Such symmetrical C-C coupling is believed to have a lower energy barrier than asymmetrical C-C coupling after a hydrogenation step, e.g., between *CO and *CHO (or *COH). The latter likely takes place at relatively high overpotentials and has been suggested as a plausible mechanism toward oxygenated hydrocarbons such as ethanol and acetate[44, 45], although *CO-*CO dimerization has also been cited to account for the selective reduction of CO to acetate.[39]

To understand the distinct catalytic selectivities of Cu-Pd alloys as compared to pure Cu, we performed density functional theory (DFT) calculations to simulate the adsorption and hydrogenation of CO on the bimetallic catalyst surfaces. The DFT calculations were performed using the Vienna Ab initio Simulation Package[46, 47] with the revised Perdew-Burke-Ernzerhof (RPBE)[48, 49] exchange-correlation functional and spin polarization. The Brillouin zone was sampled using generalized Monkhorst-Pack *k*-point grids with a minimum distance of 55 Å in corresponding real-space superlattices.[50, 51] The effect of solvation[52, 53] on the free energies of adsorbates was treated as a constant energy shift[19, 54] as deteremined from a statistical analysis of DFT calculations using the implicit solvation model implemented in VASPsol.[55] We chose (100) as the model surface considering that it is likely the most active for C-C coupling,[8, 19, 56] and DFT in the generalized gradient approximation (including RPBE) is known to predict the incorrect adsorption site for CO on Cu(111).[57, 58] To account for the disorder in the alloys, 4 randomly

ordered slabs were generated at each composition and results were reported by taking the average at each type of site over the four slabs. Standard errors of the mean were relatively small. They are reported along with the averages (see **Table S2** and **Table S4**) and shown as error bars in plots (see **Figure 4a** and **Figure S26**). Reaction energetics was evaluated using the computational hydrogen electrode model.[59, 60] Equilibrium CO coverage was determined by calculating the differential adsorption energy of CO,[61, 62] which measures the adsorption energy of the last adsorbed CO molecule at a given coverage. The coverage before this differential adsorption energy changes sign was used as the equilibrium coverage. Additional details of the computational methods are provided in Section 2 of the Supporting Information. A more comprehensive computational study of all possible reaction pathways post C-C coupling on the random Cu-Pd alloy catalysts remains challenging. This situation is different from the previous studies of bimetallic catalysts where only one type of element is considered on the surface.[27, 63] The variety of adsorption sites, possible orientations and arrangements of multi-carbon adsorbates, and multiple steps in competing pathways makes it significantly more complicated for the simulation of CO reduction toward C_2 hydrocarbons on the disordered, heteroatomic Cu-Pd surfaces. We have thus focused the present discussion on the C-C coupling mechanisms.

At the CO partial pressure of 1 atm used in the experiments, we predict the surfaces of the catalysts to be covered with ½ monolayer of CO (**Figure S23**). Previous experiments have shown that the ground state of adsorbed CO (*CO) on the Cu(100) surface at this coverage is a $c(2\times2)$ structure (**Figure S24a**) on the top sites,[64] and on the Pd(100) surface it is a $c\left(2\sqrt{2}\times\sqrt{2}\right)R\,45^{o}$ structure **(Figure S24e)** on the bridge sites.[65, 66] Both $c(2\times2)$ and $c\left(2\sqrt{2}\times\sqrt{2}\right)R\,45^{o}$ structures were considered for bridge adsorption on the bimetallic surfaces,

with $c\left(2\sqrt{2}\times\sqrt{2}\right)R\,45^{o}$ consistently found to be slightly more stable than $c(2\times2)$ for the various Cu-Pd (including Cu and Pd) surfaces. Our calculations indicate that as the Pd content in the Cu-Pd bimetallic catalysts increases, the transition from on-top to bridge adsorption takes place between Cu_3Pd_1 and Cu_1Pd_1 (**Figure 4a**; also see **Figure S25** and **Table S2** in the Supporting Information for more details). The change of CO adsorption site is predicted to have a significant effect on the energetics of CO hydrogenation. In the $c\left(2\sqrt{2}\times\sqrt{2}\right)R\,45^{o}$ configuration, the average energy for hydrogenation of *CO to *CHO (which is significantly more stable than *COH on both the top and bridge sites, see **Tables S5 and S6**) on the Cu-Pd bridge sites of the Cu_1Pd_1 surface is 113 (or 54) meV lower than that on the Cu (or Pd) top sites of the Cu_3Pd_1 surface. The corresponding difference is 228 meV (or 169 meV) in the case of $c(2\times2)$.

Further examination of the molecular configurations reveals that the reduced hydrogenation energy on the Cu-Pd bridge sites can be attributed to the enhanced stabilization of *CHO via electronic interactions between the O atom and the Cu side of the bridge, where the H atom is positioned toward the Pd side (**Figure 4b**, **Table S5**). This suggests that the *CO molecules on the Cu-Pd bridge sites of Cu_1Pd_1 and Cu_1Pd_3 are more likely to be hydrogenated than their counterparts on the top sites of Cu or Cu_3Pd surfaces (see also **Figure S26**). The unique feature of the Cu-Pd bridge sites is better illustrated in the correlation of CO hydrogenation energy to the CO adsorption energy. As shown in **Figure 4c** for the different adsorption sites on Cu_1Pd_1, the Cu-Pd bridge sites clearly deviate from the linear scaling relationship drawn for homoatomic Cu-Cu or Pd-Pd sites. Notably, this finding is in line with the alloying effect previously suggested for breaking the linear scaling relationship governing the

activity of monometallic catalysts for CO_2 reduction.[67] After a *CO on the Cu-Pd bridge site is hydrogenated, it can undergo C-C coupling with a neighboring *CO on the Cu sites to form C_2 species, which accounts for the electroreduction of CO to C_2 hydrocarbons on the Cu-Pd bimetallic catalysts (**Figure 4d**). Such asymmetrical *CO-*CHO coupling mechanism, as enabled by the heteroatomic ensembles of Cu and Pd on the bimetallic catalyst surfaces, is distinct from the symmetrical *CO-*CO dimerization mechanism taking place on Cu surfaces, which is known for selective production of ethylene.

The occurrence of *CO hydrogenation prior to C-C coupling was further supported by measurements and modeling of the CO electroreduction reaction kinetics. **Figure 5** summarizes the measured reaction orders with respect to CO (n_{CO}, at −1.0 V) and Tafel slopes (η). The dependence of $J_{acetate}$ on the CO partial pressure (P_{CO}) consistently exhibited a linear regime at lower CO partial pressures and a plateau at higher CO partial pressures. The plateau was reached at 63.3, 25.3 and 25.3 kPa for $Cu_{70}Pd_{30}$, $Cu_{49}Pd_{51}$ and $Cu_{23}Pd_{77}$, respectively. The decrease of the saturation pressure with the increase of Pd content in the bimetallic catalysts can be attributed to the stronger binding of CO, as predicted from the DFT calculations (**Figure 4a**). Before the saturation was reached, n_{CO} was determined to be nearly 1 for $Cu_{49}Pd_{51}$ and $Cu_{23}Pd_{77}$ and about 0.5 for $Cu_{70}Pd_{30}$. By performing kinetic modeling for the CO reduction reaction, we can assign the first order to surfaces in which *CO hydrogenation is relatively fast compared to *CO-*CO coupling, whereas the half order is observed when the competing *CO-*CO coupling pathway is relatively fast (see the Supporting Information for more details). The latter case is in line with the observation of more ethylene on the Cu-rich surfaces, which are likely to be derived from the *CO-*CO pathway[8] (**Figure 2a, b**). The kinetic models, DFT calculations (**Figure 4b**), and experimental reaction order data (**Figure 5**) support the idea that increasing Pd content leads to

more rapid CO hydrogenation, shifting the reaction pathway towards increased *CO-*CHO coupling.

Despite the different reaction orders with respect to CO, the Tafel slope of J_{CO} was determined to be consistently at ca. −120 mV/dec for the three alloy catalysts at saturation pressures (see the insets shown in **Figure 5**). This is because, for both pathways, the rate is limited by the first electron transfer, namely the proton coupled electron transfer (PCET) of *CO hydrogenation for the *CO-*CHO pathway and the electron transfer mediated *CO-*CO coupling in the other case.[12, 21] The combination of theoretical analysis and experimental data are thus consistent with the asymmetrical C-C coupling mechanism as presented in **Figure 4c**, which accounts for the electroreduction of CO to acetate on the Cu-Pd bimetallic catalysts. Notably, this mechanism also explains the experimentally observed trend of acetate production with respect to the alloy composition (**Figure 3b**), as the number of Cu-Pd bridge sites on a random alloy surface maximizes at the equimolar composition (**Figure S21**).

The above discussion has accounted for the unique C-C coupling mechanism on the Cu-Pd bimetallic catalysts. While the difference in C-C coupling mechanism can largely explain the suppression of ethylene formation, it remains unclear why acetate is favorably produced over ethanol. An examination of CO reduction on the bimetallic Cu-Pd catalysts in 1 mol/L $KHCO_3$ (pH = 8.4) shows that ethanol is the most favorable C_2 product, albeit with relatively low overall FEs for the multi-carbon products (up to 38% at −1.2 V vs. RHE) (**Figure S17**). This is distinct from the situation with 1 mol/L of KOH (pH = 14), where acetate was found to be dominant product (up to 65% for FE_{CH3COO^-} at -1.0 V vs. RHE). We note that, although the partial current densities toward acetate (j_{CH3COO^-}) are quite different, the partial current densities toward ethanol

($j_{CH3COOH}$) are actually quite consistent between the two cases. These results indicate that the reactivity of Cu-Pd for CO-to-ethanol conversion is pH-independent, whereas the CO-to-acetate conversion is enhanced at high electrolyte pH. This finding is consistent with the alkalinity effect reported in the electroreduction of CO to acetate on Cu.[39] It is suggested that, although the alcohol pathway shares a common *CO–*CHO intermediate, the hydroxylation of ethenone with H_2O or OH^- are unique for the acetate pathway, which is enhanced in alkaline electrolytes. Elucidation of the reaction pathways post C-C coupling on the heteroatomic surfaces toward different C_2 hydrocarbons would require much more sophisticated computational simulations and goes beyond the scope of present study.

CONCLUSION

We have investigated the electroreduction of CO on Cu-Pd bimetallic catalysts. High activity and selectivity have been demonstrated for the electrosynthesis of acetate by using gas-diffusion electrodes and flowing alkaline catholytes, achieving >65% in Faradaic efficiency and >200 mA/cm^2 in geometric current density. An asymmetrical C-C coupling mechanism via *CO-*CHO coupling has been proposed to explain the composition-dependent catalytic performances and selective reduction of CO to acetate. This mechanism was supported by the computational prediction of *CO adsorption on the bridge sites of bimetallic surfaces and correspondingly reduced CO hydrogenation barrier as compared to the on-top adsorption on Cu-rich surfaces. The proposed *CO-*CHO coupling mechanism was further supported by the first-order reaction kinetics as determined from the combined experimental and computational studies. It is noted that further investigations of the CO_2 and CO reduction electrocatalysis on such heteroatomic

surfaces of alloy catalysts can be performed by using in-situ molecular spectroscopy. More comprehensive computational simulation of the reaction pathways toward different C_2 products would also be important to understand the distinct catalytic selectivities of the bimetallic catalysts as compared to monometallic Cu.

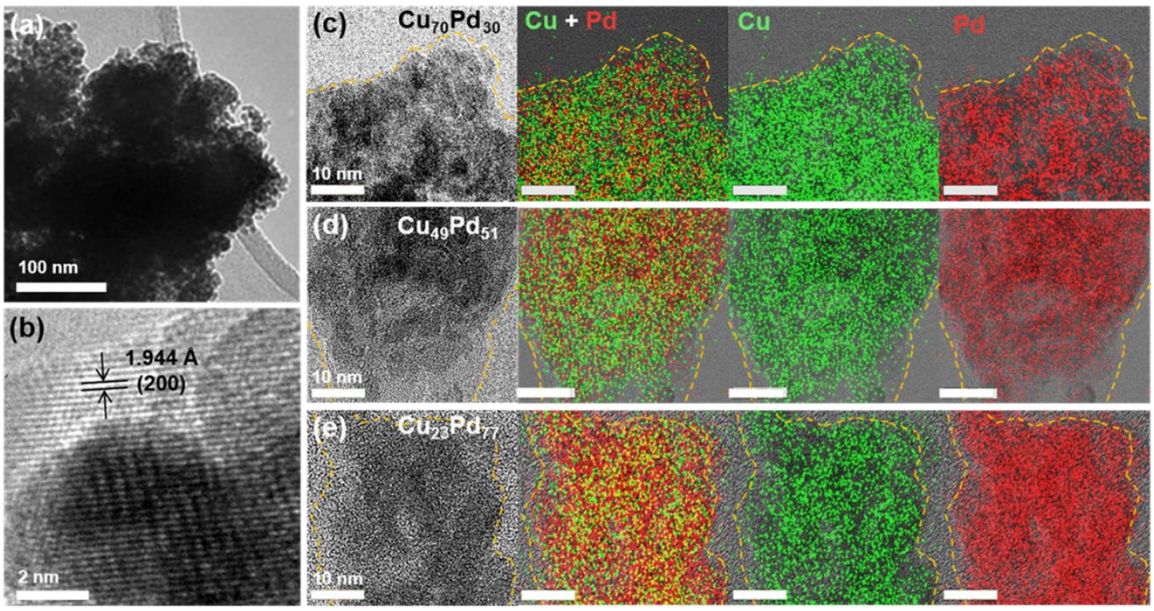

Figure 1. Characterization of the Cu-Pd bimetallic electrocatalysts. (a) Representative low- and (b) high-resolution TEM images of $Cu_{49}Pd_{51}$. (c-e) Element mapping analyses for (c) $Cu_{70}Pd_{30}$, (d) $Cu_{49}Pd_{51}$ and (e) $Cu_{23}Pd_{77}$. The green and red colors represent Cu and Pd elements, respectively.

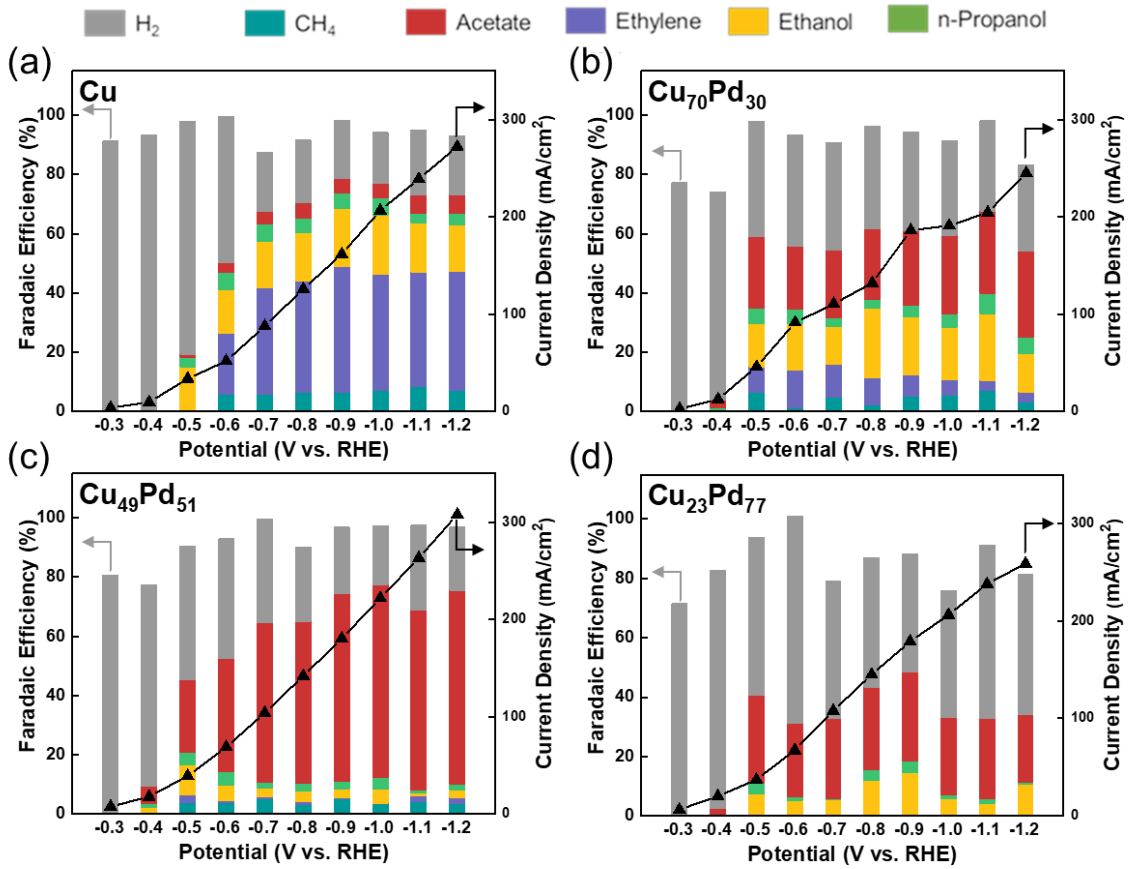

Figure 2. Summary of the Faradaic efficiencies (FEs) and geometric current densities measured for the electroreduction of CO on: (a) Cu, (b) $Cu_{70}Pd_{30}$, (c) $Cu_{49}Pd_{51}$ and (d) $Cu_{23}Pd_{77}$.

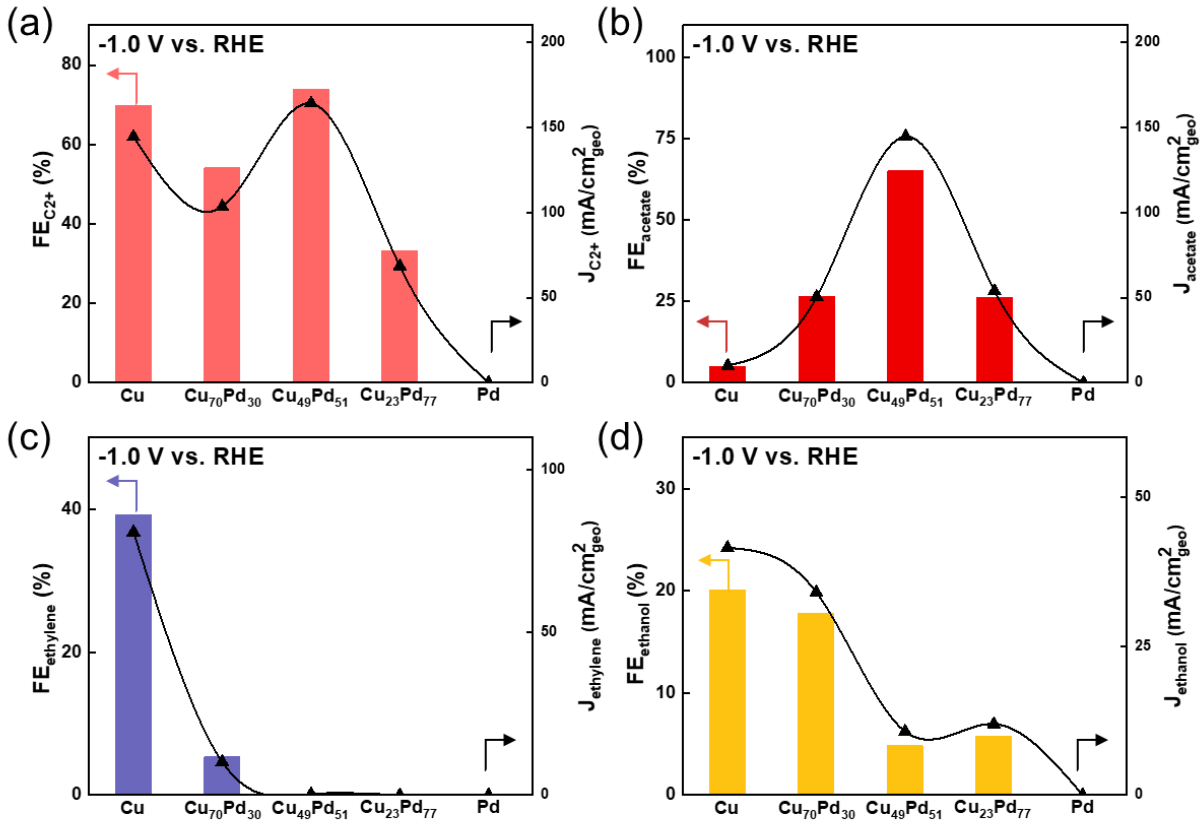

Figure 3. Comparison of the electrocatalytic performances of various catalysts for CO reduction: partial current densities and FEs (at −1.0 V) toward all C_{2+} products (a), acetate (b), ethylene (c) and ethanol (d).

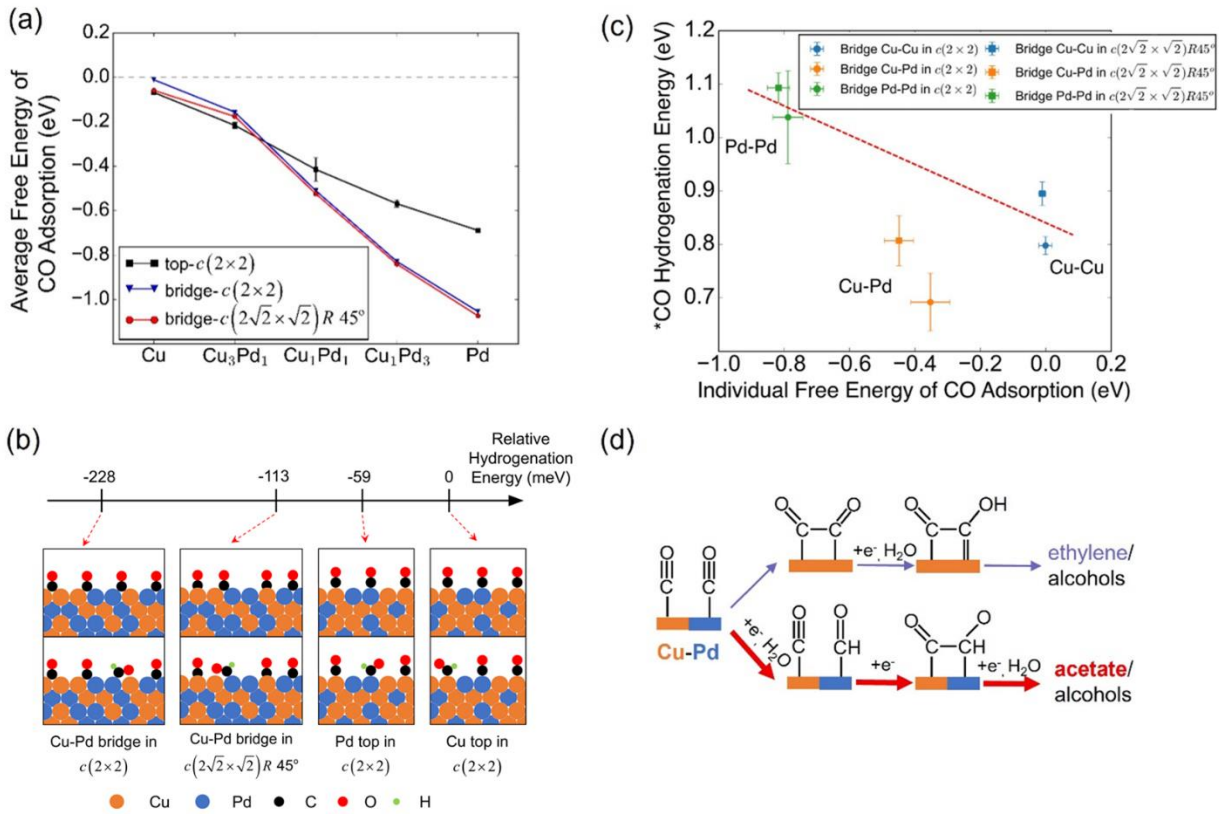

Figure 4. (a) Average free energies of CO adsorption and (b) relative hydrogenation energies for *CO on the various catalyst surfaces. Error bars in (a) represent standard errors of the mean. Numerical values are summarized in Table S2 of the SI. In (b), the left two cases are for bridge adsorption on $Cu_1Pd_1(100)$, while the right two are for $Cu_3Pd(100)$ in the on-top configuration. The calculated energies for *CO hydrogenation to *CHO are given in reference to the case of Cu top sites on $Cu_3Pd_1(100)$. (c) Correlation between CO adsorption and hydrogenation energies for the different adsorption sites on Cu_1Pd_1. Error bars represent standard errors of the mean of four random configurations. Values in this plot are listed in Table S4. (d) Proposed different C-C coupling mechanisms for the electroreduction of CO on Cu (above) and Cu-Pd alloy (below) surfaces.

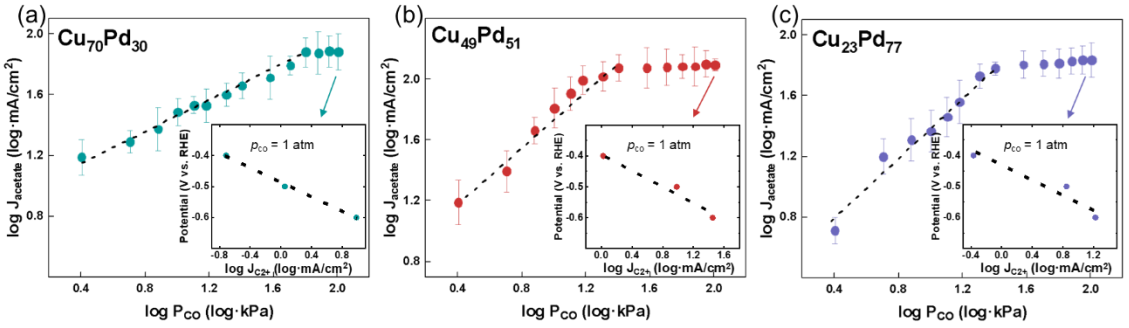

Sample	Linear Range	k	r	η (mV/dec)
$Cu_{70}Pd_{30}$	p_{CO}: 0-63.33 kPa	0.4821	0.992	118
$Cu_{49}Pd_{51}$	p_{CO}: 0-25.33 kPa	0.9546	0.990	124
$Cu_{23}Pd_{77}$	p_{CO}: 0-25.33 kPa	1.0282	0.990	114

Figure 5. Reaction orders determined at −1.0 V for the electroreduction of CO on the different bimetallic catalysts: (a) $Cu_{70}Pd_{30}$, (b) $Cu_{49}Pd_{51}$, (c) $Cu_{23}Pd_{77}$. The insets show the corresponding Tafel slopes derived from the measurements at 1 atm of CO. Error bars for the reaction order measurements represent standard deviations from three independent measurements and Tafel lines were determined with linear fit.

ASSOCIATED CONTENT

Supporting Information.

Detailed methods (synthesis, characterization, electrochemistry, DFT calculations, and kinetic analysis) and corresponding additional data (PDF)

AUTHOR INFORMATION

Corresponding Author

*chaowang@jhu.edu. (C.W.)

*tmueller@jhu.edu. (T.M.)

Author Contributions

‡H.S. and Y.W. contributed equally to this work.

ACKNOWLEDGMENT

This work is supported by National Science Foundation (CBET-1803482 and CBET-1930013) and the U.S. Department of Energy's Office of Energy Efficiency and Renewable Energy (EERE) under the Bioenergy Engineering for Products Synthesis (BEEPS) program of the Bioenergy Technologies Office (BETO) (DE-EE0008501).

REFERENCES

1. Whipple, D. T.; Kenis, P. J. A., Prospects of CO_2 utilization via direct heterogeneous electrochemical reduction. *J. Phys. Chem. Lett.* **2010,** *1* (24), 3451-3458.

2. De Luna, P.; Hahn, C.; Higgins, D.; Jaffer, S. A.; Jaramillo, T. F.; Sargent, E. H., What would it take for renewably powered electrosynthesis to displace petrochemical processes? *Science* **2019,** *364* (6438), eaav3506.

3. Xiao, H.; Cheng, T.; Goddard, W. A.; Sundararaman, R., Mechanistic explanation of the pH dependence and onset potentials for hydrocarbon products from electrochemical reduction of CO on Cu (111). *J. Am. Chem. Soc.* **2016,** *138* (2), 483-486.

4. Dinh, C. T.; Burdyny, T.; Kibria, M. G.; Seifitokaldani, A.; Gabardo, C. M.; de Arquer, F. P. G.; Kiani, A.; Edwards, J. P.; De Luna, P.; Bushuyev, O. S.; Zou, C. Q.; Quintero-Bermudez, R.; Pang, Y. J.; Sinton, D.; Sargent, E. H., CO_2 electroreduction to ethylene via hydroxide-mediated copper catalysis at an abrupt interface. *Science* **2018,** *360* (6390), 783-787.

5. Rabinowitz, J. A.; Kanan, M. W., The future of low-temperature carbon dioxide electrolysis depends on solving one basic problem. *Nat. Commun.* **2020,** *11* (1), 5231.

6. Hori, Y.; Wakebe, H.; Tsukamoto, T.; Koga, O., Electrocatalytic process of CO selectivity in electrochemical reduction of CO_2 at metal electrodes in aqueous media. *Electrochim. Acta* **1994,** *39* (11), 1833-1839.

7. Rosen, B. A.; Salehi-Khojin, A.; Thorson, M. R.; Zhu, W.; Whipple, D. T.; Kenis, P. J. A.; Masel, R. I., Ionic liquid–mediated selective conversion of CO_2 to CO at low overpotentials. *Science* **2011,** *334* (6056), 643.

8. Schouten, K. J. P.; Qin, Z.; Pérez Gallent, E.; Koper, M. T. M., Two pathways for the formation of ethylene in CO Reduction on single-crystal copper electrodes. *J. Am. Chem. Soc.* **2012,** *134* (24), 9864-9867.

9. Raciti, D.; Cao, L.; Livi, K. J.; Rottmann, P. F.; Tang, X.; Li, C.; Hicks, Z.; Bowen, K. H.; Hemker, K. J.; Mueller, T., Low-overpotential electroreduction of carbon monoxide using copper nanowires. *ACS Catal.* **2017,** *7* (7), 4467-4472.

10. Jouny, M.; Luc, W.; Jiao, F., High-rate electroreduction of carbon monoxide to multi-carbon products. *Nat. Catal.* **2018,** *1*, 748-755.

11. Raciti, D.; Wang, C., Recent advances in CO_2 reduction electrocatalysis on copper. *ACS Energy Lett.* **2018,** *3* (7), 1545-1556.

12. Li, J.; Chang, K.; Zhang, H.; He, M.; Goddard III, W. A.; Chen, J. G.; Cheng, M.-J.; Lu, Q., Effectively increased efficiency for electroreduction of carbon monoxide using supported polycrystalline copper powder electrocatalysts. *ACS Catal.* **2019,** *9* (6), 4709-4718.

13. Mistry, H.; Reske, R.; Zeng, Z.; Zhao, Z.-J.; Greeley, J.; Strasser, P.; Cuenya, B. R., Exceptional size-dependent activity enhancement in the electroreduction of CO_2 over Au nanoparticles. *J. Am. Chem. Soc.* **2014,** *136* (47), 16473-16476.

14. Morales-Guio, C. G.; Cave, E. R.; Nitopi, S. A.; Feaster, J. T.; Wang, L.; Kuhl, K. P.; Jackson, A.; Johnson, N. C.; Abram, D. N.; Hatsukade, T.; Hahn, C.; Jaramillo, T. F., Improved CO_2 reduction activity towards C_{2+} alcohols on a tandem gold on copper electrocatalyst. *Nat. Catal.* **2018,** *1* (10), 764-771.

15. Mezzavilla, S.; Horch, S.; Stephens, I. E. L.; Seger, B.; Chorkendorff, I., Structure sensitivity in the electrocatalytic reduction of CO_2 with gold catalysts. *Angew. Chem. Int. Ed.* **2019,** *58* (12), 3774-3778.

16. Lu, Q.; Rosen, J.; Zhou, Y.; Hutchings, G. S.; Kimmel, Y. C.; Chen, J. G.; Jiao, F., A selective and efficient electrocatalyst for carbon dioxide reduction. *Nat. Commun.* **2014,** *5* (1), 3242.

17. Zheng, T.; Jiang, K.; Ta, N.; Hu, Y.; Zeng, J.; Liu, J.; Wang, H., Large-Scale and Highly selective CO_2 electrocatalytic reduction on nickel single-atom catalyst. *Joule* **2018,** *3* (1), 14.

18. Wang, Y.; Su, H.; He, Y.; Li, L.; Zhu, S.; Shen, H.; Xie, P.; Fu, X.; Zhou, G.; Feng, C.; Zhao, D.; Xiao, F.; Zhu, X.; Zeng, Y.; Shao, M.; Chen, S.; Wu, G.; Zeng, J.; Wang, C., Advanced electrocatalysts with single-metal-atom active sites. *Chem. Rev.* **2020,** *120* (21), 12217–12314.

19. Calle-Vallejo, F.; Koper, M. T. M., Theoretical considerations on the electroreduction of CO to C_2 species on Cu(100) electrodes. *Angew. Chem. Int. Ed.* **2013,** *52* (28), 7282-7285.

20. Montoya, J. H.; Shi, C.; Chan, K.; Nørskov, J. K., Theoretical insights into a CO dimerization mechanism in CO_2 electroreduction. *J. Phys. Chem. Lett.* **2015,** *6* (11), 2032-2037.

21. Cheng, T.; Xiao, H.; Goddard, W. A., Full atomistic reaction mechanism with kinetics for CO reduction on Cu(100) from ab initio molecular dynamics free-energy calculations at 298 K. *Proc. Natl. Acad. Sci.* **2017,** *114* (8), 1795.

22. Garza, A. J.; Bell, A. T.; Head-Gordon, M., Mechanism of CO_2 reduction at copper surfaces: pathways to C_2 products. *ACS Catal.* **2018,** *8* (2), 1490-1499.

23. Pang, Y.; Li, J.; Wang, Z.; Tan, C.-S.; Hsieh, P.-L.; Zhuang, T.-T.; Liang, Z.-Q.; Zou, C.; Wang, X.; De Luna, P.; Edwards, J. P.; Xu, Y.; Li, F.; Dinh, C.-T.; Zhong, M.; Lou, Y.; Wu, D.; Chen, L.-J.; Sargent, E. H.; Sinton, D., Efficient electrocatalytic conversion of carbon monoxide to propanol using fragmented copper. *Nat. Catal.* **2019,** *2* (3), 251-258.

24. Jouny, M.; Hutchings, G. S.; Jiao, F., Carbon monoxide electroreduction as an emerging platform for carbon utilization. *Nat. Catal.* **2019,** *2* (12), 1062-1070.

25. Raciti, D.; Wang, C., Electrochemical alternative to Fischer-Tropsch. *Nat. Catal.* **2018,** *1* (10), 741-742.

26. Nitopi, S.; Bertheussen, E.; Scott, S. B.; Liu, X.; Engstfeld, A. K.; Horch, S.; Seger, B.; Stephens, I. E. L.; Chan, K.; Hahn, C.; Nørskov, J. K.; Jaramillo, T. F.; Chorkendorff, I., Progress and perspectives of electrochemical CO_2 reduction on copper in aqueous electrolyte. *Chem. Rev.* **2019,** *119* (12), 7610-7672.

27. Kim, D.; Xie, C.; Becknell, N.; Yu, Y.; Karamad, M.; Chan, K.; Crumlin, E. J.; Nørskov, J. K.; Yang, P., Electrochemical activation of CO_2 through atomic ordering transformations of AuCu nanoparticles. *J. Am. Chem. Soc.* **2017,** *139* (24), 8329-8336.

28. Zhu, W.; Zhang, L.; Yang, P.; Hu, C.; Dong, H.; Zhao, Z.-J.; Mu, R.; Gong, J., Formation of enriched vacancies for enhanced CO_2 electrocatalytic reduction over AuCu alloys. *ACS Energy Lett.* **2018,** *3* (9), 2144-2149.

29. Wang, L.; Higgins, D. C.; Ji, Y.; Morales-Guio, C. G.; Chan, K.; Hahn, C.; Jaramillo, T. F., Selective reduction of CO to acetaldehyde with CuAg electrocatalysts. *Proc. Natl. Acad. Sci.* **2020,** *117* (23), 12572-12575.

30. Clark, E. L.; Hahn, C.; Jaramillo, T. F.; Bell, A. T., Electrochemical CO_2 reduction over compressively strained CuAg surface alloys with enhanced multi-carbon oxygenate selectivity. *J. Am. Chem. Soc.* **2017,** *139* (44), 15848-15857.

31. Hoang, T. T.; Verma, S.; Ma, S.; Fister, T. T.; Timoshenko, J.; Frenkel, A. I.; Kenis, P. J.; Gewirth, A. A., Nanoporous copper–silver alloys by additive-controlled electrodeposition

for the selective electroreduction of CO_2 to ethylene and ethanol. *J. Am. Chem. Soc.* **2018,** *140* (17), 5791-5797.

32. Ma, S.; Sadakiyo, M.; Heima, M.; Luo, R.; Haasch, R. T.; Gold, J. I.; Yamauchi, M.; Kenis, P. J., Electroreduction of carbon dioxide to hydrocarbons using bimetallic Cu–Pd catalysts with different mixing patterns. *J. Am. Chem. Soc.* **2017,** *139* (1), 47-50.

33. Burch, R., Importance of electronic ligand effects in metal alloy catalysts. *Acc. Chem. Res.* **1982,** *15* (1), 24-31.

34. Liu, P.; Norskov, J. K., Ligand and ensemble effects in adsorption on alloy surfaces. *Phys Chem. Chem. Phys.* **2001,** *3* (17), 3814-3818.

35. Strasser, P.; Koh, S.; Anniyev, T.; Greeley, J.; More, K.; Yu, C.; Liu, Z.; Kaya, S.; Nordlund, D.; Ogasawara, H.; Toney, M. F.; Nilsson, A., Lattice-strain control of the activity in dealloyed core-shell fuel cell catalysts. *Nat. Chemistry* **2010,** *2* (6), 454-60.

36. Bai, X. F.; Chen, W.; Zhao, C. C.; Li, S. G.; Song, Y. F.; Ge, R. P.; Wei, W.; Sun, Y. H., Exclusive formation of formic acid from CO_2 electroreduction by a tunable Pd-Sn alloy. *Angew. Chem. Int. Ed.* **2017,** *56* (40), 12219-12223.

37. Sun, K.; Cheng, T.; Wu, L. N.; Hu, Y. F.; Zhou, J. G.; Maclennan, A.; Jiang, Z. H.; Gao, Y. Z.; Goddard, W. A.; Wang, Z. J., Ultrahigh mass activity for carbon dioxide reduction enabled by gold-iron core-shell nanoparticles. *J. Am. Chem. Soc.* **2017,** *139* (44), 15608-15611.

38. Wang, Y. X.; Shen, H.; Livi, K. J. T.; Raciti, D.; Zong, H.; Gregg, J.; Onadeko, M.; Wan, Y. D.; Watson, A.; Wang, C., Copper nanocubes for CO_2 reduction in gas diffusion electrodes. *Nano Lett.* **2019,** *19* (12), 8461-8468.

39. Luc, W.; Fu, X.; Shi, J.; Lv, J.-J.; Jouny, M.; Ko, B. H.; Xu, Y.; Tu, Q.; Hu, X.; Wu, J.; Yue, Q.; Liu, Y.; Jiao, F.; Kang, Y., Two-dimensional copper nanosheets for electrochemical reduction of carbon monoxide to acetate. *Nat. Catal.* **2019,** *2* (5), 423-430.

40. Chen, D.; Yao, Q.; Cui, P.; Liu, H.; Xie, J.; Yang, J., Tailoring the selectivity of bimetallic copper–palladium nanoalloys for electrocatalytic reduction of CO_2 to CO. *ACS Appl. Energy Mater.* **2018,** *1* (2), 883-890.

41. Loiudice, A.; Lobaccaro, P.; Kamali, E. A.; Thao, T.; Huang, B. H.; Ager, J. W.; Buonsanti, R., Tailoring copper nanocrystals towards C_2 products in electrochemical CO_2 reduction. *Angew. Chem. Inter. Ed.* **2016,** *55* (19), 5789-5792.

42. Goodpaster, J. D.; Bell, A. T.; Head-Gordon, M., Identification of possible pathways for C–C bond formation during electrochemical reduction of CO_2: new theoretical insights from an improved electrochemical model. *J. Phys. Chem. Lett.* **2016,** *7* (8), 1471-1477.

43. Cheng, T.; Xiao, H.; Goddard, W. A., Free-energy barriers and reaction mechanisms for the electrochemical reduction of CO on the Cu(100) surface, including multiple layers of explicit solvent at pH 0. *J. Phys. Chem. Lett.* **2015,** *6* (23), 4767-4773.

44. Schouten, K. J. P.; Pérez Gallent, E.; Koper, M. T. M., The influence of pH on the reduction of CO and CO_2 to hydrocarbons on copper electrodes. *J. Electroanal. Chem.* **2014,** *716*, 53-57.

45. Raciti, D.; Mao, M.; Park, J. H.; Wang, C., Local pH effect in the CO_2 reduction reaction on high-surface-area copper electrocatalysts. *J. Electrochem. Soc.* **2018,** *165* (10), F799-F804.

46. Kresse, G.; Furthmuller, J., Efficient iterative schemes for ab initio total-energy calculations using a plane-wave basis set. *Phys. Rev. B* **1996,** *54* (16), 11169-11186.

47. Kresse, G.; Furthmuller, J., Efficiency of ab-initio total energy calculations for metals and semiconductors using a plane-wave basis set. *Comp. Mater. Sci.* **1996,** *6* (1), 15-50.

48. Perdew, J. P.; Burke, K.; Ernzerhof, M., Generalized gradient approximation made simple. *Phys.Rev. Lett.* **1996,** *77* (18), 3865-3868.

49. Hammer, B.; Hansen, L. B.; Nørskov, J. K., Improved adsorption energetics within density-functional theory using revised Perdew-Burke-Ernzerhof functionals. *Phys. Rev. B* **1999,** *59* (11), 7413-7421.

50. Wisesa, P.; McGill, K. A.; Mueller, T., Efficient generation of generalized Monkhorst-Pack grids through the use of informatics. *Phys. Rev. B* **2016,** *93* (15), 155109.

51. Wang, Y.; Wisesa, P.; Balasubramanian, A.; Dwaraknath, S.; Mueller, T., Rapid generation of optimal generalized Monkhorst-Pack grids. *Comp. Mater. Sci.* **2020**, 110100.

52. Tomasi, J.; Mennucci, B.; Cammi, R., Quantum mechanical continuum solvation models. *Chem. Rev.* **2005,** *105* (8), 2999-3094.

53. Garcia-Ratés, M.; López, N., Multigrid-based methodology for implicit solvation models in periodic DFT. *J. Chem. Theory Comput.* **2016,** *12* (3), 1331-1341.

54. Hansen, H. A.; Shi, C.; Lausche, A. C.; Peterson, A. A.; Nørskov, J. K., Bifunctional alloys for the electroreduction of CO_2 and CO. *Phys. Chem. Chem. Phys.* **2016,** *18* (13), 9194-9201.

55. Mathew, K.; Sundararaman, R.; Letchworth-Weaver, K.; Arias, T. A.; Hennig, R. G., Implicit solvation model for density-functional study of nanocrystal surfaces and reaction pathways. *J. Chem. Phys.* **2014,** *140* (8), 084106.

56. Jiang, K.; Sandberg, R. B.; Akey, A. J.; Liu, X.; Bell, D. C.; Nørskov, J. K.; Chan, K.; Wang, H., Metal ion cycling of Cu foil for selective C–C coupling in electrochemical CO_2 reduction. *Nat. Catal.* **2018,** *1* (2), 111-119.

57. Gajdoš, M.; Hafner, J., CO adsorption on Cu (111) and Cu (001) surfaces: improving site preference in DFT calculations. *Surf. Sci.* **2005,** *590* (2-3), 117-126.

58. Gameel, K. M.; Sharafeldin, I. M.; Abourayya, A. U.; Biby, A. H.; Allam, N. K., Unveiling CO adsorption on Cu surfaces: new insights from molecular orbital principles. *Phys. Chem. Chem. Phys.* **2018,** *20* (40), 25892-25900.

59. Nørskov, J. K.; Rossmeisl, J.; Logadottir, A.; Lindqvist, L.; Kitchin, J. R.; Bligaard, T.; Jónsson, H., Origin of the overpotential for oxygen reduction at a fuel-cell cathode. *J. Phys. Chem. B* **2004,** *108* (46), 17886-17892.

60. Peterson, A. A.; Abild-Pedersen, F.; Studt, F.; Rossmeisl, J.; Norskov, J. K., How copper catalyzes the electroreduction of carbon dioxide into hydrocarbon fuels. *Energ. Environ. Sci.* **2010,** *3* (9), 1311-1315.

61. Nørskov, J. K.; Studt, F.; Abild-Pedersen, F.; Bligaard, T., *Fundamental concepts in heterogeneous catalysis*; John Wiley & Sons, 2014; pp 26-45.

62. Huang, Y.; Handoko, A. D.; Hirunsit, P.; Yeo, B. S., Electrochemical reduction of CO_2 using copper single-crystal surfaces: effects of CO* coverage on the selective formation of ethylene. *ACS Catal.* **2017,** *7* (3), 1749-1756.

63. Kim, D.; Resasco, J.; Yu, Y.; Asiri, A. M.; Yang, P., Synergistic geometric and electronic effects for electrochemical reduction of carbon dioxide using gold–copper bimetallic nanoparticles. *Nat. Commun.* **2014,** *5* (1), 1-8.

64. Andersson, S.; Pendry, J. B., Structure of CO adsorbed on Cu(100) and Ni(100). *Phys. Rev. Lett.* **1979,** *43* (5), 363-366.

65. Tracy, J. C.; Palmberg, P. W.; C., T. J.; W., P. P., Structural influences on adsorbate binding energy. I. carbon monoxide on (100) palladium. *J. Chem. Phys.* **1969,** *51* (11), 4852-4862.

66. Behm, R. J.; Christmann, K.; Ertl, G.; Hove, M. A. V.; L., P. R.; H., M. H., Adsorption of CO on Pd(100). *J. Chem. Phys.* **1980,** *73* (6), 2984-2995.

67. Peterson, A. A.; Nørskov, J. K., Activity descriptors for CO_2 electroreduction to methane on transition-metal catalysts. *J. Phys. Chem. Lett.* **2012,** *3* (2), 251-258.

Table of Content